fine-grained microcrystalline Si_3N_4 product produced after an additional short period of spark-discharge milling. Silicon can be nitrided in ammonia by conventional magneto-ball milling under low-energy shearing conditions to form an amorphous-like product[10]. The powder can then be hot-pressed to form monolithic microcrystalline Si_3N_4. However, the more direct route of hot-pressing microcrystalline Si_3N_4 that is produced by discharge milling may be more attractive because such Si_3N_4 is less likely to oxidize during processing and because there is no requirement to remove hydrogen.

Spark-discharge milling was successfully employed for initiation of reduction processes. Results obtained for haematite are shown in Fig. 5. We used pre-milled powder, magneto-milled under conventional impact mode in air. After 20 h, XRD indicated broad peaks corresponding to nanostructural haematite. This powder was subsequently milled for 30 min in nitrogen under spark milling conditions, resulting in formation of magnetite or maghaematite. As indicated by the associated SEMs, the corresponding change in particle morphology is from clumps of nanocrystalline powder (Fig. 5a) to finer particles containing coarser, submicrometre crystallites (Fig. 5b).

There are promising applications of this electrical discharge method for materials and minerals processing. Handling of ultrafine ball milled powders with large surface areas is generally difficult owing to their high susceptibility to structural changes, particularly oxidation, even in inert atmospheres containing only trace impurities such as water vapour or oxygen. Such problems may potentially be overcome if discharge-assisted milling can be applied for the direct formation of more stable phases. A general method might involve conventional milling to produce a reactive ultrafine or nanostructural product followed by final milling under an electrical discharge to generate particular heat-induced transformations, such as recrystallization, grain growth, relaxation of internal stresses or the direct formation of new phases by solid–solid reaction. Such a technique may avoid problems associated with handling and subsequent treatment of highly reactive powders. Areas of minerals processing which might benefit from scaled-up versions of discharge-assisted milling range from more energy-efficient methods of ore fracturing to alternative routes of minerals reduction. □

Received 29 September 2001; accepted 16 July 2002; doi:10.1038/nature00985.

1. Zoz, H. Attritor technology—latest developments. *Mater. Sci. Forum* **179–181,** 419–424 (1995).
2. Koch, C. C. Materials synthesis by mechanical alloying. *Annu. Rev. Mater. Sci.* **18,** 121–143 (1989).
3. Basset, D., Matteazzi, P. & Mani, F. Designing a high energy ball-mill for synthesis nanophase materials in large quantities. *Mater. Sci. Eng. A* **A168,** 149–152 (1993).
4. Pelletier, J. *et al.* New trends in DECR plasma technology: applications to novel duplex treatments and process combinations with extreme plasma specifications. *Surf. Coat. Technol.* **139,** 222–232 (2001).
5. Takaki, K., Taguchi, D. & Fujiwara, T. Voltage–current characteristics of high-current glow discharges. *Appl. Phys Lett.* **78,** 2646–2648 (2001).
6. Mishra, R. S. & Mukherjee, A. K. Electric pulse assisted rapid consolidation of ultrafine grained alumina matrix composites. *Mater. Sci. Eng. A* **A287,** 178–182 (2000).
7. El-Eskandarany, M. S., Sumijama, K., Aoki, K. & Suzuki, K. Syntheses of full-density nanocrystalline titanium nitride compacts by plasma-activated sintering of mechanically reacted powder. *Met. Mater. Trans. A* **29A,** 1973–1981 (1998).
8. Calka, A. & Radlinski, A. P. Universal high performance ball milling device and its application for mechanical alloying. *Mater. Sci. Eng.* **A134,** 1350–1353 (1991).
9. Wexler, D., Calka, A. & Colburn, S. J. Rapid sintering of nanostructural powder to form Si_3N_4. *Mater. Sci. Forum* **269–272,** 219–224 (1998).
10. Li, Z. L., Williams, J. S. & Calka, A. The role of hydrogen and iron in silicon nitridation by ball milling. *J. Appl. Phys.* **81,** 8028–8034 (1997).

Acknowledgements

We acknowledge R. deJong, R. Kinnell and S. Selby for their contributions towards construction of the discharge milling devices. We are especially grateful to D. Dunne for his support and leadership. This project was supported by funding from the Australian Research Council.

Competing interests statement

The authors declare that they have no competing financial interests.

Correspondence and requests for materials should be addressed to A.C. (e-mail: aoc2107@uow.edu.au).

Acceleration of rain initiation by cloud turbulence

G. Falkovich*, A. Fouxon* & M. G. Stepanov*†

** Physics of Complex Systems, Weizmann Institute of Science, Rehovot 76100, Israel*

† Institute of Automation and Electrometry, Novosibirsk 630090, Russia

Vapour condensation in cloud cores produces small droplets that are close to one another in size. Droplets are believed to grow to raindrop size by coalescence due to collision[1,2]. Air turbulence is thought to be the main cause for collisions of similar-sized droplets exceeding radii of a few micrometres, and therefore rain prediction requires a quantitative description of droplet collision in turbulence[1–5]. Turbulent vortices act as small centrifuges that spin heavy droplets out, creating concentration inhomogeneities[6–14] and jets of droplets, both of which increase the mean collision rate. Here we derive a formula for the collision rate of small heavy particles in a turbulent flow, using a recently developed formalism for tracing random trajectories[15,16]. We describe an enhancement of inertial effects by turbulence intermittency and an interplay between turbulence and gravity that determines the collision rate. We present a new mechanism, the 'sling effect', for collisions due to jets of droplets that become detached from the air flow. We conclude that air turbulence can substantially accelerate the appearance of large droplets that trigger rain.

The local distribution of droplets over sizes, $n(a,t,\mathbf{r}) = n(a)$, changes with condensation and coalescence according to refs 1, 2 (see Table 1 for definitions of variables):

$$\frac{\partial n(a)}{\partial t} = -q\frac{\partial}{\partial a}\frac{n(a)}{a} - \frac{\partial}{\partial \mathbf{r}}\mathbf{v}n + \int \mathrm{d}a'\left[\frac{K(a',a'')n(a')n(a'')}{2(a''/a)^2} - K(a',a)n(a')n(a)\right] \quad (1)$$

Here, $\mathbf{v}(t, \mathbf{r})$ is the droplet velocity at point $\mathbf{r}$ at time t, q is proportional to the supersaturation and the diffusivity of the vapour and $a'' = (a^3 - a'^3)^{1/3}$. The collection kernel is proportional to the collision kernel, which is the product of the target area and the relative velocity Δv of droplets before the contact: $K(a_1, a_2) \simeq \pi(a_1 + a_2)^2\Delta v$. For droplets larger than couple of micrometres across, brownian motion can be neglected and the collision kernel in still air is due to gravitational settling[1,2]: $K_g(a_1, a_2) = \pi(a_1 + a_2)^2 E(a_1, a_2)|u_g(a_1) - u_g(a_2)|$. When the Reynolds number of the flow around the droplet, $\mathrm{Re}_a \equiv u_g a/\nu$, is not too large and concentration is small enough ($na^3\mathrm{Re}_a^{-2} \ll 1$) the settling velocity is due to the balance of gravity and friction: $u_g = g\tau$ with the Stokes time $\tau = (2/9)(\rho_0/\rho)(a^2/\nu)$. Here ρ_0, ρ are water and air densities respectively. Hydrodynamic interaction between approaching droplets is accounted for in K_g by the collision efficiency E, for which values can be found in refs 1, 17.

Cloud condensation nuclei are typically of micrometre or submicrometre size and the initial stage of droplet growth is solely due to condensation: $n(a,t) = af(a^2 - 2qt)$ with the function f determined by the initial distribution. An important conclusion is that while the distribution shifts to larger sizes, it keeps its small width over a^2 (a few micrometres squared or less). It would take many hours for condensation to grow millimetre-size raindrops, especially with the account of vapour depletion. Such growth is supposed to come from coalescence but because $K_g \propto |a_1^2 - a_2^2|$ the gravitational collision rate is strongly suppressed for droplets that are close in size. With narrow local size distributions in cloud cores, rain would not start in still air for many hours. There is then the

long-standing problem of the bottleneck in the transition from condensation to coalescence stage[1–5,8–11,18–20] which we discuss here.

In some cases, droplets with substantially different sizes may appear, owing to the existence of ultra-giant nuclei[18,19]. Another possibility that we consider here is that turbulence-induced collisions[8–11,20] may occur. Both velocity and concentration of droplets fluctuate in a random flow. To provide meteorology with an effective computational tool, theoretical physics is expected to produce the condensation–coagulation equation (1) averaged over space. Here we derive analytically the averaged equation—that is, we obtain the effective collision kernel $\bar{K} = \langle K(a_1, a_2) n_1 n_2 \rangle / \langle n_1 \rangle \langle n_2 \rangle$]—and solve it numerically to demonstrate the changes in the average distribution $n(a, t)$ brought about by turbulence.

For the basic discussion of cloud turbulence see the reviews in refs 3–5 and the references therein. Turbulence intensity can be characterized by the energy input rate ε which determines the root-mean-square (r.m.s.) velocity gradient: $\lambda \simeq (\varepsilon/\nu)^{1/2}$. We consider small droplets with the Stokes number $\mathrm{St} = \lambda\tau$ (which characterizes mean droplet inertia) smaller than unity. If inertia is neglected, droplets follow the incompressible air flow and their concentration is uniform. Droplet motion in the air flow gradient s then provides $\Delta v \simeq s(a_1 + a_2)$ and gives the mean collision kernel[20] $\langle K_t \rangle \simeq \lambda (a_1 + a_2)^3$. Inertia deviates droplets from the air flow, adding a contribution to Δv proportional to τs the mean value of which is St, that is, small[20]. Hence Saffman and Turner[20] concluded that only extremely energetic turbulence with $\varepsilon > 2{,}000\,\mathrm{cm^2\,s^{-3}}$ would produce a noticeable collision kernel. We note, however, that it is $\bar{K}$ rather than $\langle K \rangle$ that determines the mean collision rate. Inertial deviation of droplets from the air flow leads to fluctuations in droplet concentration, characterized by the factor $k_{12} = \langle n_1 n_2 \rangle / \langle n_1 \rangle \langle n_2 \rangle > 1$, which may be large. Concentration fluctuations have been observed in experiments and numerical simulations[5–12] and described analytically for same-size droplets in low Reynolds flow without gravity[13,14]: $k(a, a) = \langle n^2 \rangle / \langle n \rangle^2 \simeq (\eta/a)^{\mathrm{St}^2}$, where $\eta \approx (\nu^3/\varepsilon)^{1/4}$ is the mean correlation scale of velocity gradients.

The Reynolds number of cloud turbulence is $\mathrm{Re} = uL/\nu$, where u is air velocity and L is the outer scale comparable to the cloud size. In the atmosphere, Re is large (10^6–10^8), that is, turbulence is intermittent and the statistics is very non-gaussian, with a substantial probability of gradients far exceeding λ. The role of gravity can be characterized by the ratio of the small-scale turbulent velocity to the settling velocity[12,21] $\epsilon \equiv (\varepsilon\nu)^{1/4}/u_g$; this parameter can be both larger and smaller than unity for $a = 1$–$100\,\mu\mathrm{m}$ and $\lambda = 1$–$20\,\mathrm{s^{-1}}$.

Here we derive the factor k_{12} for droplets under gravity in high-Re flow. We show that contribution of large gradients can significantly increase k_{12} compared with the low-Re case and that gravity provides for a sharp maximum of k_{12} at $a_1 = a_2$. We also describe a new inertial mechanism of collisions due to rare events with large gradients ($s \simeq \tau^{-1} \gg \lambda$) that produce jets of droplets initially accelerated by the air flow and then detached from it. That gives an additive contribution K_i into $\bar{K}$. We call this the 'sling effect' and show that turbulence intermittency can make K_i substantial even at small St. No realistic direct numerical simulations are possible for droplets in high-Re turbulence, so analytical derivations are indispensable. We derive $\bar{K}(\epsilon, \mathrm{St}, \mathrm{Re})$ and show that the turbulence-induced collision rate can be substantial even for small droplets in moderate turbulence when St is small.

The field $\mathbf{v}(\mathbf{r}, t)$ giving the velocity of a droplet located at $\mathbf{r}$ at time t satisfies the equation[6,22] $\partial_t \mathbf{v} + (\mathbf{v}\nabla)\mathbf{v} = (\mathbf{u} - \mathbf{v})/\tau + g\boldsymbol{z}$, where $\boldsymbol{z}$ is a unit vector pointing downwards. The gradients $\sigma = \nabla\mathbf{v}$ and $s = \nabla\mathbf{u}$ taken at a droplet's trajectory are related as follows: $\dot{\sigma} + \sigma^2 = (s - \sigma)/\tau$. When $|\sigma| \ll \tau^{-1}$, it has a smooth evolution determined by $\sigma(t) = \int^t \mathrm{d}t' \exp[(t' - t)/\tau] s(t')/\tau$. If, however, $|\sigma| > \tau^{-1}$ then the inertial term σ^2 dominates and may lead to an explosive evolution $\sigma(t) \propto (t_0 - t)^{-1}$ that produces shock in $\mathbf{v}(\mathbf{r})$ and singularities in $n(\mathbf{r})$.

The probability P of an explosive event is that of large and persistent gradients s. The correlation time $\tau_c(s)$ of the air flow gradient is given by the minimum between the turnover time $|s|^{-1}$ and the time $l(s)/u_g$ needed for droplets to cross the region $l(s) \simeq \sqrt{\nu/|s|}$ over which s is correlated. The gradient s that leads to $|\sigma| \simeq \tau^{-1}$ must either exceed the threshold described by the extrapolation formula $s_b = [\tau^{-2} + \lambda^2\epsilon^{-4}]^{1/2}$ or be larger than $1/\tau$ and occupy the region in space $l(s_b)s_b/s$. Because the only available data are on the single-point probability density function (PDF) $\mathscr{P}(s)$ we estimate the probability of explosion from below: $P \equiv \int_{1/\tau}^{\infty} P(|\sigma|)\,\mathrm{d}|\sigma| \simeq \tau s_b \int_{s_b} \mathscr{P}(|s|)\,\mathrm{d}|s|$, where the prefactor τs_b appears because $s > s_b$ can occur at any moment within the interval τ. Once a fluctuation with a negative eigenvalue $\sigma_i < -\tau^{-1}$ occurs, the inertial term σ^2 exceeds the driving term s_i/τ and the friction term $-\sigma_i/\tau$, which corresponds to a free motion of droplets along the direction of σ_i on a timescale of order τ. A negative velocity gradient means that faster droplets catch up with slower ones, creating a cubic singularity[23] in the relation between the current coordinate $x(t)$ and the initial one y: $x = y^3/3l^2 - yt/\tau$. Here $l = l(s_b)$ is the correlation length of $|\sigma| = 1/\tau$ and t is counted from the moment of singularity. Using $n(x, t) = n(y)|\partial y/\partial x|$ and $|\sigma| = |(\partial\mathbf{v}/\partial y)(\partial y/\partial x)| \simeq \tau^{-1}|\partial y/\partial x|$ we find the contribution of the preshocks ($t < 0$) into the collision rate: $\langle |\sigma| n^2 \rangle \simeq P\tau^{-1} \int \mathrm{d}x \int_{-\bar{t}}^{0} \mathrm{d}t (\partial y/\partial x)^3 \langle n^2(y) \rangle / l\tau \simeq P\tau^{-1}(l/a)^{1/3} \langle \tilde{n}^2[a(l/a)^{2/3}] \rangle$. Formula $\langle |\sigma| n^2 \rangle$ assumes smoothness over the scale a, so we introduced $\tilde{n}[\delta y]$ coarse-grained over δy, taking $\delta y \simeq a(l/a)^{2/3}$, which corresponds to $\delta x \simeq a$.

After the shock ($t > 0$), folds appear in the map $y(x)$ in the region $|x| < 2l(t/\tau)^{3/2}/3$: for every x value there are three y values which correspond to the three groups of droplets that came from different places and have different velocities. Nearby droplets from the same group have $\Delta v \simeq \sigma a$ and contribute $\langle |\sigma| n^2 \rangle \simeq P\tau^{-1}(l/a)^{1/2} \langle \tilde{n}^2[(la)^{1/2}] \rangle$. However, this contribution and that of preshocks are both less than that given by collisions of droplets from different groups. Groups coming from afar appear because droplets

Table 1 **Parameters**

Quantity	Units	Description
$n(a)$	$\mathrm{cm^{-4}}$	Distribution of droplets over sizes in a unit volume
a	cm	Droplet radius
t	s	Time
$\mathbf{r}$	cm	Spatial coordinate
q	$\mathrm{cm^2\,s^{-1}}$	Rate of condensational growth
K	$\mathrm{cm^3\,s^{-1}}$	Collision kernel
u_g	$\mathrm{cm\,s^{-1}}$	Terminal fall velocity
g	$\mathrm{cm\,s^{-2}}$	Acceleration of gravity
ν	$\mathrm{cm^2\,s^{-1}}$	Air viscosity
ε	$\mathrm{cm^2\,s^{-3}}$	Energy dissipation rate per unit mass
$\mathbf{u}(\mathbf{r}, t)$	$\mathrm{cm\,s^{-1}}$	Air velocity

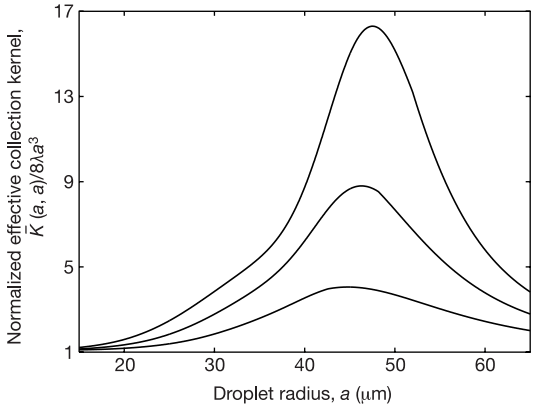

Figure 1 Normalized effective collection kernel for equal-size droplets at $\mathrm{Re} \simeq 10^6$ according to equations (2), (3), (4) and (6). From bottom to top, $\lambda = 10$, 15 and $20\,\mathrm{s^{-1}}$.

are shot out of curved streamlines with too high a centrifugal acceleration, an effect known to anyone who has used a sling to throw stones. That is why we call this the 'sling effect'. Droplets separated at the beginning of the free motion by a distance $\simeq l$ have $\Delta v \simeq l/\tau$ and provide for the inertial collision kernel:

$$K_i(a_1, a_2) \simeq \pi(a_1 + a_2)^2 E'(P_1 l_1/\tau_2 + P_2 l_2/\tau_2)/2. \qquad (2)$$

Subscripts denote different droplet sizes, $\tau(a_1) = \tau_1$, $P_1 = P(|\sigma| > 1/\tau_1)$. Because the velocities and the concentrations of the different groups are uncorrelated, $\langle K_i(a_1, a_2) n_1 n_2\rangle = K_i(a_1, a_2)\langle n_1\rangle\langle n_2\rangle$. The collision efficiency E' in equation (2) can be expressed via E taken for the effective sizes, giving the same Δv. We thus obtain $E' \approx 0.93$–0.98 in the interval 15–100 μm for collinear velocities (non-collinearity further increases E'; ref. 3), so with our accuracy, $E' \approx 1$. We note that $K_i(a, a)$ is larger than the contribution due to droplets from the same group by the factor $\sqrt{l/a}\langle\tilde{n}^2[l]\rangle/\langle\tilde{n}^2[(la)^{1/2}]\rangle$. It is shown below that $\langle\tilde{n}^2[r]\rangle \propto r^{-\alpha}$ with $\alpha < 1$ so that K_i indeed dominates. The ratio $K_i/\lambda a^3 \simeq P\mathrm{St}^{-1}(l/a)$ has the smallness of P compensated by two large factors and can exceed unity even at small St. Most importantly, $K_i(a, a) \neq 0$.

We now describe concentration fluctuations and derive k_{12}. Because of inertia, the divergence of $\mathbf{v}$ is nonvanishing[6], albeit small: $\mathrm{tr}\sigma = -\int \exp[(t' - t)/\tau]\mathrm{tr}\sigma^2(t')\,\mathrm{d}t' \ll |\sigma|$ at $\tau|\sigma| \ll 1$. Negative $\mathrm{tr}\sigma^2$ corresponds to elliptic flows (vortices) which act as centrifuges decreasing n. Droplets concentrate in hyperbolic regions (between the vortices) where $\mathrm{tr}\sigma^2 > 0 > \mathrm{tr}\sigma$. Clusters of droplets are created with sizes not exceeding η, as follows from theory[13,14] and as seen in numerics[24] and observations[25]. We note in passing that as clusters do not exceed η the fluctuations of droplet concentration do not produce significant fluctuations in vapour concentration (because the vapour diffusivity is comparable to the air viscosity) so that droplet distribution over sizes cannot be significantly broadened during the condensation stage; see also ref. 26. Clustering can be readily understood: a compressible flow with lagrangian chaos creates a fractal concentration, the so-called Sinai–Ruelle–Bowen measure[16]. The moments of the fractal measure behave as powers of the scale ratio: $\langle\tilde{n}[r]^\beta\rangle \simeq \langle n\rangle^\beta(\eta/r)^{\gamma(\beta)}$, where $\gamma(\beta)$ is convex and $\gamma(0) = \gamma(1) = 0$. As $\gamma'(0)$ is negative[13] (it is proportional to the sum of the backward-in-time Lyapunov exponents of the $\mathbf{v}$-flow), then $\alpha \equiv \gamma(2) > 0$. Droplets of different sizes have additional relative velocity $|\tau_1 - \tau_2|(g + \lambda^2\eta)$ that stops clustering at $r \simeq |\tau_1 - \tau_2|(g + \lambda^2\eta)/\lambda_\mathrm{d}$. We thus find:

$$k_{12} \simeq \langle\tilde{n}_1(a)\tilde{n}_2(a)\rangle/(\langle n_1\rangle\langle n_2\rangle)$$
$$\simeq [a/\eta + (\lambda + g/\lambda\eta)|\tau_1 - \tau_2|\epsilon^{-1}]^{-\alpha} \qquad (3)$$

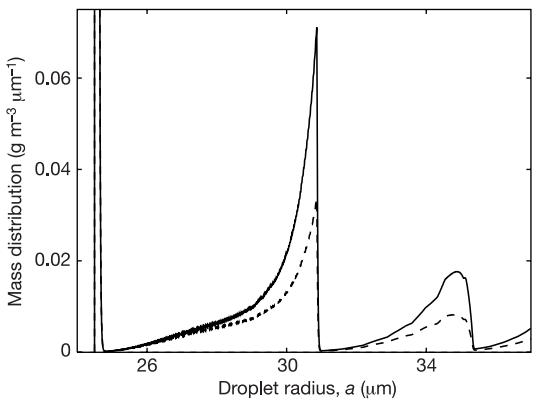

Figure 2 Distribution over sizes after 10 min. The dashed line is the solution of equation (1) with the mean-field collision kernel and the solid line is the solution of equation (1) with equation (4).

We distinguish a_1 from a_2 only in $|\tau_1 - \tau_2|$ giving the sharpest dependence. The exponent α is described by equation (6), derived in the Methods section below. For sufficiently small droplets ($\mathrm{St} < 1$ and $\epsilon > 1$) and not very high Re, we have $\alpha \simeq \mathrm{St}^2 F_3$, where $F_3 \approx \lambda^{-3}\int |s|^3\mathscr{P}(s)\,\mathrm{d}s$ is a growing function of Re that describes how turbulence intermittency amplifies the effect of small droplet inertia. At low Re and $\mathrm{St} < 1$, α does not depend on ϵ, so the only dependence $k_{11}(\epsilon)$ can come from shock contribution and has to be weak (logarithmic), which agrees with numerics[12]. At large Re, both α and k_{12} have a maximum at $\mathrm{St} \simeq \epsilon^2$.

We now write the effective collision kernel for small heavy particles in turbulence:

$$\bar{K}(a_1, a_2) \simeq k_{12}\lambda(a_1 + a_2)^3 + k_{12}K_g + K_i \qquad (4)$$

To compare with numerics done for low Re without gravity[9,10] we use equations (2), (3), (4) and (6) with $P \simeq \exp(-\mathrm{St}^{-2})$ and $l \simeq \eta\mathrm{St}^{1/2}$. Analytics and numerics agree well, showing fast growth of $\bar{K}$ with St at $\mathrm{St} < 1$ and a (broad) maximum at $a_1 = a_2$ (refs 9, 10). As St approaches unity, $k_{12} \gg 1$ and $K_i \gg \lambda(a_1 + a_2)^3$, which explains the observation[9] that contributions of both preferential concentration and relative velocity are important. Gravity suppresses K_i increasing s_b at $\epsilon^2 < \mathrm{St}$. It also makes k_{12} a sharp function of $|a_1 - a_2|$ so that the gravitational collision rate is only weakly enhanced by preferential concentration, because $k_{12} > 1$ where $K_\mathrm{g} \approx 0$. At small St, we can also neglect the turbulence-induced increase of the vertical flux[12].

For practical applications to high-Re flows, α and K_i have to be evaluated with $\mathscr{P}(s)$ determined experimentally. To make an estimate from below, we numerically evaluate equations (2), (3), (4) and (6) for moderate turbulence with $\mathrm{Re} \simeq 10^6$, taking $\mathscr{P}(s)$ from ref. 27. Figure 1 shows the effective collision kernel $\bar{K}$ normalized by $8\lambda a^3$. The normalized kernel has a maximum at $\mathrm{St} \simeq \epsilon^2$ which corresponds to the balance between inertia and gravity when the Stokes time τ is the universal value $(\nu/g^2)^{1/3}$. Droplets of such size take time τ to fall through the vortex with a turnover time τ. The effect of centrifugal force is less both for smaller droplets (which are less inertial) and for larger ones (which spend less time inside the vortex). This is to be contrasted with the maximum at $\mathrm{St} \simeq 1$ in low-Reynolds numerics without gravity[9,10]. How inertia and gravity influence droplet settling is discussed in refs 12, 21, 28; see also refs 29, 30 on the role of turbulence.

We see that the interplay between gravity and turbulence intermittency makes inertial enhancement of the turbulence-induced collision rate significant only in the restricted interval of droplet sizes that depends on the air density (between 20 and 60 μ for $\rho = 10^{-3}\,\mathrm{g\,cm^{-3}}$). The condensation–coagulation bottleneck is expected precisely in this interval, so turbulence must be able to alleviate it. To illustrate the effect, we solve space-averaged equation (1) numerically with the mean-field collection kernels $K_\mathrm{g} + \langle K_\mathrm{t}\rangle$ (dashed line in Fig. 2) and with $\bar{K}$ (solid line in Fig. 2) for $\lambda = 20\,\mathrm{s}^{-1}$, $\eta = 6$ mm and $q = 5 \times 10^{-9}\,\mathrm{cm^2\,s^{-1}}$. We took 50 droplets per cm^3 with initial sizes in the interval 2–3 μm. Even for such relatively low level of turbulence and small size of droplets, the difference in coalescence-produced secondary peaks is apparent after only 10 min. The main peak is at $a = 25$ μm. The number density of coalescence-produced droplets is $1.06\,\mathrm{cm}^{-3}$ with the newly found $\bar{K}$ versus $0.64\,\mathrm{cm}^{-3}$ with the old mean-field values.

We thus conclude that turbulence-induced inertial effects can substantially accelerate the transition from condensation to coalescence stage in the interval of few tens of micrometres. Our results are valid for a low concentration of small droplets and not very energetic turbulence, conditions compatible with the data for most clouds[1,2,4,5], so we believe that equations (2), (3), (4) and (6) provide for an effective tool in rain prediction. □

Methods

To determine α from equation (3) we consider[13] the prehistory of a cluster with the

smallest size r. It is formed by a gradual deformation of an η-size region with an initially uniform concentration. The shock contribution to the moment, $\langle \tilde{n}^2[r]\rangle \propto \int dx(\partial y/\partial x)^2 \propto \ln(l/r)^{1/2}$, contains a logarithm that is of order unity in our case. Therefore, we neglect shocks and consider fluctuations with $|\sigma| < \tau^{-1}$. The smallest size of the region evolves as $\eta \exp[\lambda_d t]$, where λ_d is the most negative Lyapunov exponent estimated as $|\lambda_d| \simeq \int dt\langle \mathrm{tr}\sigma^T(0)\sigma(t)\rangle \simeq \lambda\epsilon\tilde{} = \lambda\epsilon(1+\epsilon^2)^{-1/2}$. Therefore, concentration fluctuations accumulate during the time $\ln(\eta/r)/|\lambda_d|$. Because $\dot{n} = -n\mathrm{tr}\sigma$ in the droplets' frame and the contribution of each cluster to the spatial average is proportional to its volume $\exp[\int_0^t \mathrm{tr}\sigma(t')\,dt']$, we obtain:

$$\langle \tilde{n}^2[r]\rangle = \langle n\rangle^2 \left\langle \exp\left[-\int_0^{\ln(\eta/r)/\lambda_d} \mathrm{tr}\sigma(t')\,dt'\right]\right\rangle$$

$$= \langle n\rangle^2 \left\langle \exp\left[\tau\int_0^{\ln(\eta/r)/\lambda_d} \mathrm{tr}\sigma^2(t')\,dt'\right]\right\rangle = \langle n\rangle^2 \left(\frac{\eta}{r}\right)^{\alpha}, \text{ for } \alpha$$

$$\simeq \tau^2/|\lambda_d| \int dt\langle\langle \mathrm{tr}\sigma^2(0)\mathrm{tr}\sigma^2(t)\rangle\rangle \quad (5)$$

where we assumed that $\ln(\eta/r)/|\lambda_d|$ is much larger than the correlation time of $\mathrm{tr}\sigma^2$. The higher terms of the cumulant expansion cannot be parametrically larger than the estimate (5) since they contain integrals estimated as $\langle\langle \tau\mathrm{tr}\sigma^2[\tau\tau_c(\sigma)\mathrm{tr}\sigma^2]^{2m+1}\rangle\rangle$, for $m \geq 1$, and both the correlation time $\tau_c(\sigma)$ and τ are less than $|\sigma|^{-1}$ in the integration domain. Moreover, if $\langle \tau^2\tau_c(\sigma)(\mathrm{tr}\sigma^2)^2\rangle$ is determined by $|\sigma| \ll \tau^{-1}$ then equation (5) is correct not only parametrically but also numerically. To evaluate α we express it via the single-time PDF $P(|\sigma|)$:

$$\alpha \simeq (\tau^2/\lambda\epsilon)\int_{\tau|\sigma|<1} d\sigma\sigma^4\tau_c(\sigma)P(|\sigma|) \quad (6)$$

To relate $P(\sigma)$ to $\mathscr{P}(s)$ measured experimentally we note that $\tau_c(s) > \tau$ for $s < s_* = \tau^{-1}\min\{1, \epsilon^2/\mathrm{St}\}$ so that $P(|\sigma|) = P(|s| = |\sigma|)$ there. At $s > s^*$ the fluctuations of s contributing to $P(\sigma)$ have $\tau_c(s) < \tau$ and can occur at any moment within τ. The extrapolation formulas are $P(|\sigma|) = (1 + \sigma^2/s_*^2)\mathscr{P}(|s| = |\sigma| + \sigma^2/s_*)$ and $\tau_c(|\sigma|) = \tau + (|\sigma| + \lambda^{1/2}|\sigma|^{1/2}\epsilon^{-1})^{-1}$. Our theory is valid as long as $\mathrm{St}\min\{1, \epsilon\} < 1$.

Received 28 February; accepted 11 July 2002; doi:10.1038/nature00983.

1. Pruppacher, H. & Klett, J. *Microphysics of Clouds and Precipitation* (Kluwer, Dordrecht, 1998).
2. Seinfeld, J. & Pandis, S. *Atmospheric Chemistry and Physics* (Wiley, New York, 1998).
3. Pinsky, M., Khain, A. & Shapiro, M. Stochastic effects of cloud droplet hydrodynamic interaction in a turbulent flow. *Atmos. Res.* **53,** 131–169 (2000).
4. Jonas, P. Turbulence and cloud microphysics. *Atmos. Res.* **40,** 283–306 (1996).
5. Vaillancourt, P. A. & Yau, M. K. Review of particle-turbulence interactions and consequences for cloud physics. *Bull. Am. Met. Soc.* **81,** 285–298 (2000).
6. Maxey, M. R. The gravitational settling of aerosol particles in homogeneous turbulence and random flow field. *J. Fluid Mech.* **174,** 441–465 (1987).
7. Squires, K. & Eaton, J. Measurements of particle dispersion from direct numerical simulations of isotropic turbulence. *J. Fluid Mech.* **226,** 1–35 (1991).
8. Pinsky, M. & Khain, A. Turbulence effects on droplet growth and size distribution in clouds—a review. *J. Aerosol Sci.* **28,** 1177–1214 (1997).
9. Sundaram, S. & Collins, L. Collision statistics in an isotropic particle-laden turbulent suspension. *J. Fluid Mech.* **335,** 75–109 (1997).
10. Zhou, Y., Wexler, A. & Wang, L.-P. Modelling turbulent collision of bidisperse inertial particles. *J. Fluid Mech.* **433,** 77–104 (2001).
11. Reade, W. & Collins, L. Effect of preferential concentration on turbulent collision rates. *Phys. Fluids* **12,** 2530–2540 (2000).
12. Wang, L. P. & Maxey, M. Settling velocity and concentration distribution of heavy particles in homogeneous isotropic turbulence. *J. Fluid Mech.* **256,** 27–68 (1993).
13. Balkovsky, E., Falkovich, G. & Fouxon, A. Intermittent distribution of inertial particles in turbulent flows. *Phys. Rev. Lett.* **86,** 2790–2793 (2001).
14. Brumfiel, G. How raindrops form. *Phys. Rev. Focus* **7,** story 14 (22 March 2001), http://focus.aps.org/v7/st14.html..
15. Shraiman, B. & Siggia, E. Scalar turbulence. *Nature* **405,** 639–646 (2000).
16. Falkovich, G., Gawedzki, K. & Vergassola, M. Particles and fields in fluid turbulence. *Rev. Mod. Phys.* **73,** 913–975 (2001).
17. Pinsky, M., Khain, A. & Shapiro, M. Collision efficiency of drops in a wide range of Reynolds numbers. *J. Atmos. Sci.* **58,** 742–766 (2001).
18. Johnson, D. B. The role of giant and ultragiant aerosol particles in warm rain initiation. *J. Atmos. Sci.* **39,** 448–460 (1982).
19. Levin, Z., Wurzler, S. & Reisin, T. Modification of mineral dust particles by cloud processing and subsequent effects on drop size distribution. *J. Geophys. Res.* **105,** 4501–4512 (2000).
20. Saffman, P. & Turner, J. On the collision of drops in turbulent clouds. *J. Fluid Mech.* **1,** 16–30 (1956).
21. Raju, N. & Meiburg, N. The accumulation and dispersion of heavy particles in forced two-dimensional mixing layers. *Phys. Fluids* **7,** 1241–1264 (1995).
22. Maxey, M. R. & Riley, J. J. Equation of motion for a small rigid sphere in a nonuniform flow. *Phys. Fluids* **26,** 883–889 (1983).
23. Vekshtein, G. *Physics of Continuous Media: A Collection of Problems with Solutions* 93–94 (Adam Hilger, Bristol, 1992).
24. Grits, B., Pinsky, M. & Khain, A. Formation of small-scale droplet concentration inhomogeneity in a turbulent flow as seen from experiments with an isotropic turbulence model. *Proc. 13th Int. Conf. on Clouds and Precipitation* Vol. 1, 138–141 (Am. Met. Soc., Reno, 2000).
25. Kostinski, A. & Shaw, R. Scale-dependent droplet clustering in turbulent clouds. *J. Fluid Mech.* **434,** 389–398 (2001).
26. Brenguier, J.-L. & Chaumat, L. Droplet spectra broadening in cumulus clouds. *J. Atmos. Sci.* **58,** 628–641 (1999).
27. Belin, F., Maurer, J., Tabeling, P. & Willaime, H. Velocity gradient distribution in fully developed turbulence: an experimental study. *Phys. Fluids* **9,** 3843–3850 (1997).
28. Davila, J. & Hunt, J. C. R. Settling of small particles near vortices and in turbulence. *J. Fluid Mech.* **440,** 117–145 (2001).
29. Crowe, C. T., Chung, J. N. & Troutt, T. R. *Particulate Two Phase Flow* Ch. 18 (ed. Roce, M. C.) 626 (Butterworth-Heinemann, Oxford, 1993).
30. Marble, F. E. Dynamics of dusty gases. *Annu. Rev. Fluid Mech.* **2,** 397–461 (1970).

Acknowledgements

We thank A. Khain, V. Lebedev and M. Pinsky for discussions, and the Minerva and Israel Science Foundations for support.

Competing interests statement

The authors declare that they have no competing financial interests.

Correspondence and requests for materials should be addressed to G.F. (e-mail: fnfal@wicc.weizmann.ac.il).

Macroecological patterns of phytoplankton in the northwestern North Atlantic Ocean

W. K. W. Li

Biological Oceanography Section, Bedford Institute of Oceanography, Department of Fisheries and Oceans, Dartmouth, Nova Scotia B2Y 4A2, Canada

Many issues in biological oceanography are regional or global in scope[1]; however, there are not many data sets of extensive areal coverage for marine plankton. In microbial ecology, a fruitful approach to large-scale questions is comparative analysis[2,3] wherein statistical data patterns are sought from different ecosystems, frequently assembled from unrelated studies[4]. A more recent approach termed macroecology characterizes phenomena emerging from large numbers of biological units by emphasizing the shapes and boundaries of statistical distributions, because these reflect the constraints on variation[5]. Here, I use a set of flow cytometric measurements to provide macroecological perspectives on North Atlantic phytoplankton communities. Distinct trends of abundance in picophytoplankton and both small and large nanophytoplankton underlaid two patterns. First, total abundance of the three groups was related to assemblage mean-cell size according to the 3/4 power law of allometric scaling in biology[6,7]. Second, cytometric diversity[8] (an ataxonomic measure of assemblage entropy) was maximal at intermediate levels of water column stratification[9]. Here, intermediate disturbance shapes diversity through an equitable distribution of cells in size classes, from which arises a high overall biomass. By subsuming local fluctuations, macroecology reveals meaningful patterns of phytoplankton at large scales.

The data were collected from 23 oceanographic cruises spanning a 13-year period. We have published previously a description of the 14 earlier cruises (1989–98), a map of the stations, and sampling methods[10]. More recently (1999–2001), we re-occupied the stations on the Scotian shelf in spring and autumn, and the Labrador Sea in spring. Although stations were located across seven biogeochemical provinces[1], only measurements in the four northwestern ones, representing 82% of the data set, were included in the present analysis. These four contiguous provinces were Atlantic Arctic (ARCT), boreal polar (BPLR), northwest Atlantic shelves (NWCS) and Gulf Stream (GFST). The stations were in an area bounded approximately by 38° N, 61° N, 42° W and 67° W. The extracted data